Publications of the Astronomical Society of the Pacific, 129:035005 (22pp), 2017 March
doi:10.1088/1538-3873/129/973/035005

A Satellite Survey of Cloud Cover and Water Vapor in the Southwestern USA and Northern Mexico

E. Carrasco[1], R. Avila[2], A. Erasmus[3,7], S. G. Djorgovski[4], A. R. Walker[5], and R. Blum[6]
[1] Instituto Nacional de Astrofísica, Óptica y Electrónica, Tonantzintla, Pue. 72840, México
[2] Centro de Física Aplicada y Tecnología Avanzada, Universidad Nacional Autónoma de México, A.P. 1-1010, Querétaro, Qro. 76000, México
[3] South African Astronomical Observatory, Cape Town 7925, South Africa
[4] Astronomy Department, California Institute of Technology, Pasadena, CA 9115, USA
[5] Cerro Tololo Inter-American Observatory, National Optical Astronomy Observatory, Casilla 603, La Serena, Chile
[6] National Optical Astronomy Observatory, Tucson, AZ 85719, USA
Received 2016 September 5; accepted 2016 October 22; published 2017 February 13

Abstract

Cloud cover and water vapor conditions in the southwestern USA and northern Mexico were surveyed as a preparatory work for the Thirty Meter Telescope (TMT) in situ site testing program. Although the telescope site is already selected, the TMT site testing team decided to make public these results for its usefulness for the community. Using 58 months of meteorological satellite observations between 1993 July and 1999 September, different atmospheric parameters were quantified from data of the 10.7 μm and of 6.7 μm windows. In particular, cloud cover and water vapor conditions were identified in preferred areas. As a result of the aerial analysis, 15 sites of existing and potential telescope were selected, compared, and ranked in terms of their observing quality. The clearest sites are located along the spine of the Baja peninsula and into southern California on mountain peaks above the temperature inversion layer. A steep gradient of cloudiness was observed along the coast where coastal cloud and fog are trapped below the inversion layer. Moving from west to east over the continent, a significant increase in cloudiness was observed. The analysis shows that San Pedro Mártir, San Gorgonio Mountain and San Jacinto Peak have the largest fraction of clear sky conditions ($\sim$74%). The site with the optimal combination of clear skies and low precipitable water vapor is Boundary Peak, Nevada. An approach based in satellite data provided a reliable method for sites comparison.

Key words: site testing – atmospheric effects

Online material: color figures

1. Introduction

In 2002, the University of California and the California Institute of Technology undertook the California Extremely Large Telescope (CELT) project aimed to build a 30-m diameter ground-based telescope for astronomy at visible and infrared wavelengths Nelson & Mast (1999); Nelson (2000). The CELT with the Very Large Telescope and the Giant Segmented Mirror Telescope merged to create the Thirty Meter Telescope (TMT) project. In 2009 July, the board of directors of the TMT Observatory Corporation selected Maunakea as the preferred site for the TMT. As described by Schöck et al. (2009), this decision officially ended the TMT site-testing work after five years of in situ measurements during which at least 2.5 annual cycles of data were acquired on each of the five candidate sites. The practical work at the sites was preceded by several years of preparatory work, most notably a series of satellite data studies of the cloud cover and the precipitable water vapor (PWV) of sites in Chile, southwestern North America, and Hawaii, on the basis of which the candidate sites were selected. The meticulous research campaigns to help guide the site-selection process for the final candidates site are discussed in several articles referred by Schöck et al. (2009). A public database of the multi-year campaign at the five candidate sites was released.[8]

Additionally, the TMT site-testing team agreed to make public the results of the preparatory work, as they can also be useful for site testers, astronomers, and other interested users around the world. In this paper, we described the analysis and results of that preparatory satellite survey of the southwestern USA and northern Mexico, based in the determination of cloud cover and PWV. This work uses the results of a study by Andre Erasmus, who tragically passed away before this paper was written. The study was carried out by Erasmus & van Staden (2002), under a contract funded by the CELT project and the data they used purchased by Cerro Tololo Inter-American

[7] Deceased.

[8] http:sitedata.tmt.org

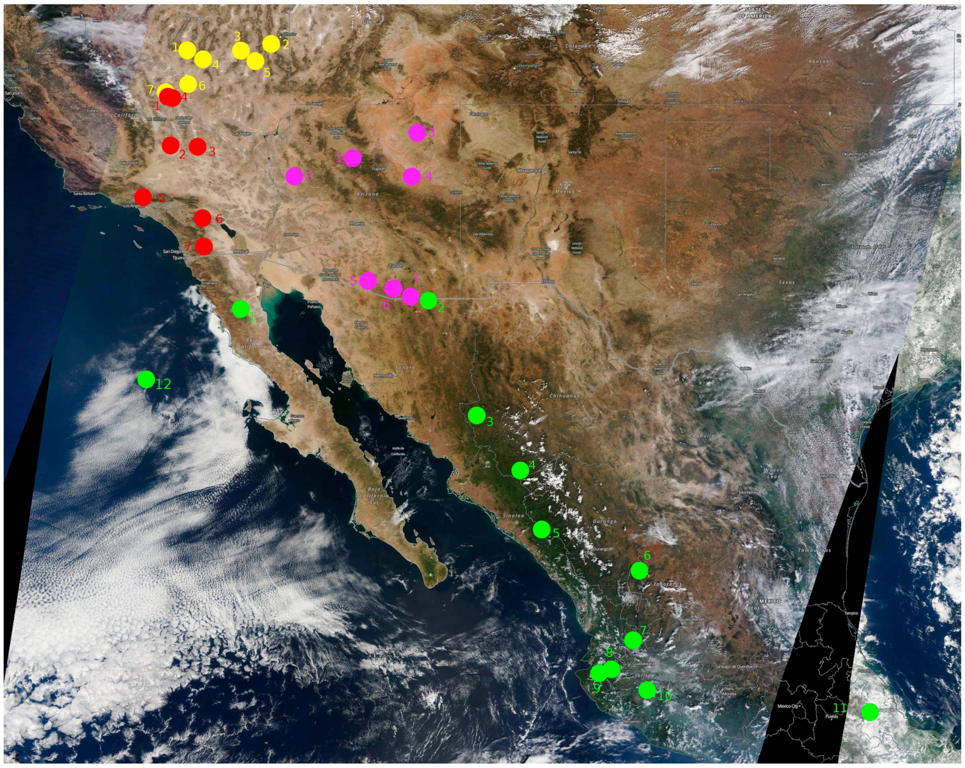

Figure 1. Sites selected for the area analysis. In California (red), Arizona (pink), Nevada (yellow), and Mexico (green). The sites' coordinates and elevations are shown in Tables 1 and 2. Courtesy of NASA Worldview.
(A color version of this figure is available in the online journal.)

Observatory (CTIO, National Optical Astronomy Observatory), the University of Tokyo, and the European Southern Observatory.

Section 2 describes the climatology, topography, and satellite data used in the analysis of the area of study. In Section 3, the methodologies to estimate the fraction of time when the sky is clear and to calculate PWV are discussed. Section 4 discusses the results, represented by maps, of the area analysis where 33 sites were initially considered. From these results, 15 sites were selected for further analysis. Section 5 discusses the results for the selected sites, obtained from the analysis of overall conditions, seasonal, and diurnal variability. Section 6 presents the summary and conclusions.

2. The Data

The study area covers 18°N to 40°N and 96°W to 124°W, as shown Figure 1. It has numerous mountain peaks with altitude, shape, and orientation potentially suitable for locating large telescopes.

2.1. Climatology Data

The preliminary site selection was based on precipitation, climatology, and topography exclusively. The mean annual precipitation data from the southwestern USA were obtained from the National Atlas of the United States (see Figure 2). The corresponding information for the sites located in Mexico was compiled from the Perry Castañeda Library Map collection[9], see Figure 3. The minimum precipitation area extends from about 37° at the California-Nevada border more or less southward to the border of Mexico. In northern Mexico, the dry zone extends into Baja and Sonora. Precipitation enhancement occurs along the Sierra Madre Occidental, but dry pockets are observed between the west coast and the cordillera even as far south as 20°. Another dry area is observed east of the Sierra Madre Occidental, due to a rain shadow effect created by the mountains.

Elevation is needed to ensure that the site lies above the temperature inversion layer that exists at the interface between air that is sinking from the tropopause level -at about 12 km- and air that is near the surface. Locations above the height of the inversion layer tend to remain free of moisture and/or dust from the surface. The height of the inversion layer varies diurnally, seasonally, and geographically, but in order that a site is above the inversion layer as frequently as possible, sites should be as high as possible. Therefore, a minimum altitude of

[9] www.lib.utexas.esu/maps

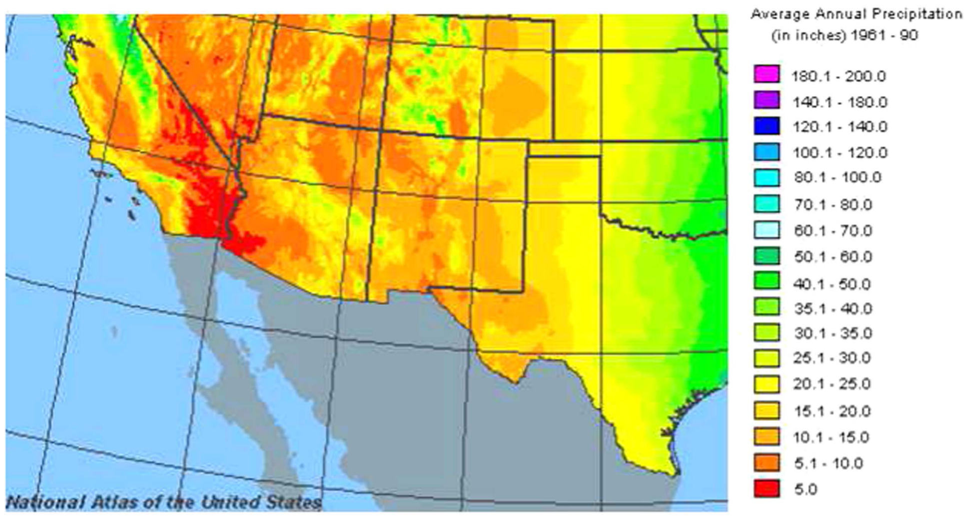

Figure 2. Mean annual precipitation for the southwestern USA for the period 1961–1990. From: *National Atlas of the United States*. Image produced by the U.S. Geological Survey.
(A color version of this figure is available in the online journal.)

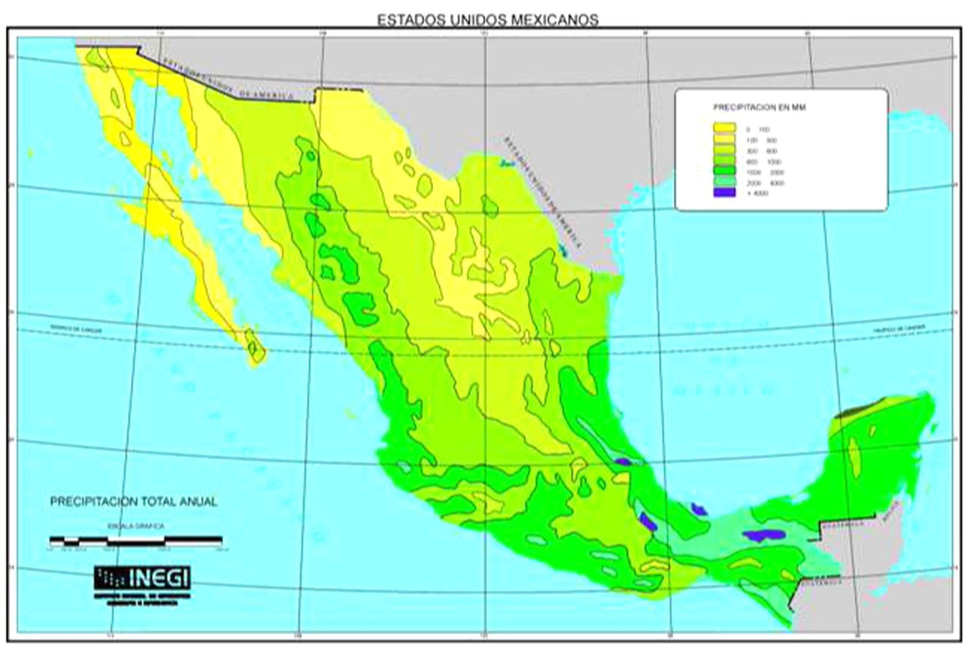

Figure 3. Mean annual precipitation for Mexico. From: *Perry Castañeda Library Map collection*. Source: INEGI.
(A color version of this figure is available in the online journal.)

2000 m was specified. Exceptions were made in the case of some existing observatories and sites close to the ocean where the inversion layer height is considerably lower. When two or more sites were found in close proximity, preference was given to the higher site. The elevation and coordinates of the sites selected for the area analysis are presented in Tables 1 and 2. Seven sites are in California, seven in Arizona, seven in Nevada, and 12 in Mexico.

2.2. Satellite Data

The satellite images used in the study are from the International Satellite Cloud Climatology Project (ISCCP). Data were derived from two satellites. Meteosat-3 from 1993 July 1 to 1995 January 31, and GOES-8 from 1995 February 1 to 1999 August 31. There is a 15-month gap in between 1996 March and 1997 May. The data were purchased from the National Climatic Data Center (NCDC) by CTIO, University of

Table 1
Preliminary Sites in California and Arizona

Location	Altitude m	Latitude N deg	Longitude W deg
California			
1. White Mountain Peak	4343	37.63	118.25
2. Olancha Peak	3696	36.27	118.12
3. Telescope Peak	3369	36.17	117.09
4. Junipero Serra	2397	37.67	118.14
5. Mt. Pinos	2692	34.81	119.15
6. San Gorgonio Mountain	3503	34.10	116.83
7. Palomar Mountain[a]	1871	33.31	116.86
Arizona			
1. Kendrick Peak	3176	35.41	111.85
2. Hualapai Peak	2566	35.08	113.90
3. Baldy Peak	3476	33.91	109.56
4. Mt. Graham[a]	3268	32.70	109.87
5. Kitt Peak[a]	2097	31.96	111.60
6. Mt. Wrightson	2882	31.70	110.85
7. Miller Peak	2886	31.39	110.29

Note.
[a] Existing observatory.

Table 2
Preliminary Sites in Nevada and Mexico

Location	Altitude m	Latitude N deg	Longitude W deg
Nevada			
1. South Shoshone Peak	3065	39.06	117.56
2. Wheeler Peak	3983	38.99	114.31
3. White Pine Peak	3098	38.87	115.46
4. Mt. Jefferson S. Summit	3640	38.75	116.93
5. Shingle Peak	2995	38.51	114.93
6. Lone Mountain	2777	38.02	117.49
7. Boundary Peak	4007	37.85	118.35
Mexico			
1. San Pedro Mártir[a]	2800	31.04	115.47
2. Cerro San José	2645	31.26	109.99
3. Cerro la Bufa	2955	27.90	107.93
4. Cerro Mohinora	3992	26.10	107.07
5. Cerro San Rafael	2971	24.30	106.10
6. Cerro Candelaria	3080	23.42	103.72
7. Cerro Yesca	2800	21.32	104.05
8. Cerro Comalito	2687	20.50	104.60
9. Cerro Desmoronado	2740	20.35	104.98
10. Nevado de Colima	4265	19.55	103.63
11. Sierra Negra[a]	4581	18.98	97.30
12. Isla de Guadalupe	1298	29.00	118.27

Note.
[a] Existing observatory.

Tokyo, and the European Southern Observatory for use in an earlier study by Erasmus & van Staden (2001).

Full-Earth scans are scheduled every three hours, although the cancellation of one or more images per day occurs periodically due to satellite housekeeping procedures, satellite maneuvers, and eclipse events. The data for the study area were extracted from the full-Earth scans and compiled in a separate database. The data are classified as highest spatial resolution by ISCCP. Raw GOES-8 data are 1 km × 1 km resolution in the visible, 4 km × 4 km in the infrared window channel and effectively 8 km × 8 km in the water vapor channel. The raw data are sampled so that the effective pixel resolution for all channels is 9.1 km × 8.0 km at Nadir.

2.3. Rawinsonde Data

At several locations within the study area, balloons carrying instrument packages are released between two (00UT and 12UT) and four (additionally 06UT and 18UT) times per day. The 29 primary stations listed in Table 3 have at least two soundings per day. Fifteen other stations with intermittent or less frequent data were also used in the analysis. It should be noted that there are few island-based radiosonde stations in the ocean areas, and all of these are not primary stations. This does have an effect on the reliability of the analysis in these areas as discussed on Section 3.

2.4. Topography Data

The height of the terrain is required to estimate surface temperatures from the rawinsonde data. Digital heights equivalent to ∼1 km vertical resolution were obtained from the United States Geological Survey. Since the pixel size in the satellite images is approximately 10 km × 10 km, several points lie (∼100) within the area corresponding to one pixel. For each location, the heights were determined by setting the site height equal to the maximum of the 36 closest points within a 5 km × 5 km square. The higher terrain, including some peaks, was well-reproduced.

3. Methodology

3.1. Definitions Day/Night Divisions and Seasons

Day/night divisions were based on true solar time or local mean time. The computational method is that presented by Sarazin (1991) and Erasmus (2000). *Day* is the period from one hour after true local sunrise time to one hour before true sunset time. *Night* is the period starting one hour after true sunset time to one hour before true sunrise time. Further divisions into day1, day2, night1, and night2 are done by dividing the applicable period exactly in half. The analysis was performed

Table 3
Primary Rawinsonde Stations

No.	Station	Latitude	Longitude
1c	Albuquerque	35.05	−122.22
2	Amarillo	35.23	−101.7
3	Oakland	37.75	−122.22
4	Del Rio	29.37	−100.92
5	Denver	39.77	−104.88
6	Dodge City	37.77	−99.97
7	Flagstaff	35.23	−111.82
8	Fort Worth	32.8	−97.3
9	Grand Junction	39.12	−108.53
10	Midland	31.93	−102.2
11	Mirimar	32.87	−117.15
12	Reno	39.57	−119.8
13	Salt Lake	40.77	−111.97
14	Tucson	32.12	−110.93
15	Vandenberg AFB	34.75	−120.57
16	Yuma	32.87	−114.33
17	Mazatlan	23.18	−106.42
18	La Paz	24.07	−110.33
19	Guadalajara	20.68	−103.33
20	Edwards AFB	34.9	−117.92
21	Manzanillo	19.07	−104.33
22	Veracruz	19.17	−96.12
23	Bakersfield	35.43	−119.03
24	Brownsville	25.9	−97.43
25	Corpus Christi	27.8	−97.5
26	Desert Rock	36.62	−116.02
27	Guaymas	27.95	−110.8
28	Oklahoma City	35.23	−97.47
29	Santa Teressa	31.9	−106.7

for different seasons and periods of the day. Seasons were defined on a climatological basis. Winter as December, January, and February (DJF); spring as March, April, and May (MAM); summer as June, July, and August (JJA); and fall as September, October, and November (SON).

3.2. Conversion of Radiance to Brightness Temperature

Meteosat-3 and GOES-8 perform real-time calibrations of infrared detectors onboard the satellite using sensor readings from dark space and reference blackbodies. Calibration coefficients thus derived are used to compute radiance values from the raw counts.

Weinreb et al. (1997) described the operational in-orbit calibration of GOES-8 and -9 imagers. Users receive scaled radiances in a variable format data stream. The authors describe the procedure and the corresponding coefficients users must apply to transform counts into radiances and from radiance into brightness temperatures for each channel. The calibration and interpretation of infrared data for all the GOES satellites are available.[10]

[10] http://www.ospo.noaa.gov/Operations/GOES/calibration

3.3. Conversion of 6.7 μm Brightness Temperature to Humidity

Water vapor in the atmosphere is absorbent at most infrared wavelengths. The absorptivity for a given wavelength determines the layer in the atmosphere in which out-going terrestrial radiation will be absorbed and re-emitted by resident water vapor. The sensitivity or weighting function for emission at 6.7 μm channel reaching the satellite, reported by Soden & Bretherton (1996), peaks strongly at about 400 mbar i.e., these observations are sensitive to emissions in the layer between 600 mbar and 300 mbar approximately. Emission from this layer depends on the amount of water vapor and temperature in the layer and is typically calibrated in terms of the relative humidity.

PWV is a quantity indicating the absolute humidity in the atmosphere above some predetermined altitude such as the surface or a constant pressure level. The PWV contained in a layer bounded by pressures p_1 and p_2 can be obtained from

$$PWV = \frac{1}{g}\int_{p_1}^{p2} xdp, \tag{1}$$

where x is the mixing ratio, the mass of water vapor per mass of air, dp is the incremental pressure change with height in Pascals, and g is the gravity acceleration constant.

The mixing ratio can be calculated as

$$x = UTH \times x_s, \tag{2}$$

where UTH is the upper tropospheric humidity and x_s is the saturation mixing ratio. UTH corresponds to the mean relative humidity of a layer extending approximately from 600 to 300 mbar. UTH values are derived from brightness temperature at 6.7 μm. x_s is the maximum water vapor carrying capacity of the air at a given temperature and pressure and it is calculated from radiosondes measurements of local temperature and pressure. Once the x profile is obtained, then PWV is calculated from Equation (1).

For GOES data, Soden & Bretherton (1993) developed a semi-empirical model in which under clear skies, the brightness temperature at 6.7 μm is proportional to the natural logarithm of the relative humidity averaged over a deep layer centered in the upper troposphere -between 600 and 300 mbar approximately- divided by the cosine of the viewing zenith angle. In this pressure interval, a constant relative humidity equal to the UTH is assumed and the mixing ratio x at each level of 10 mbar is calculated from Equation (2).

The values from 600 to 300 mbar were respectively scaled to higher and lower pressure levels using the daily radiosonde sounding for the closest station and time. The mixing ratios x profiles exhibit good linearity with pressure levels above 600 mbar and below 300 mbar the contribution is very small as shown by the Denver mean monthly mixing ratio profiles for four months of 1993 reported by Erasmus & Sarazin (2002). Erasmus & van Staden (2001) also present a plot for the Antofagasta radiosonde for the 10-year period where the mean monthly mixing ratio shows the same behavior.

3.3.1. Validation

To demonstrate the validity of this method, observations of PWV made from the ground at Mt. Graham were compared with those from the satellite for the same period. 225 GHz radiometer data were obtained from the Submillimeter Telescope Observatory (SMTO). The data are observations of atmospheric opacity every half hour for 24 hours. Precise conversion from opacity to PWV requires the use of an atmospheric model and upper-air meteorological data. At SMTO, a conversion factor of 19 is being used for on-site applications (Dumke 2002, private communication), so this value was adopted for the purposes of this comparison. The comparison was based on observations in the period 1997 June to 1998 May. The SMTO data includes observations made when clouds are present. To facilitate comparison with the satellite observations that are made strictly under clear conditions, an attempt was made to remove cloudy records by placing an upper limit on radiometer PWV values. It is not possible to know exactly what the value of PWV will be when clouds are present, as this depends on the air temperature and altitude of the clouds.

Based on experience forecasting PWV at La Silla Observatory, the highest PWV value observed in the absence of clouds is about 17 mm. Adjusting this limit to the higher Mt. Graham site altitude, the corresponding value would be an upper limit of 13 mm, so clouds may be present for lower PWV values. Figure 4 shows the PWV monthly average from the satellite and ground data. By considering only radiometer values less than 7 mm, the discrepancy between satellite and radiometer data disappears and the balance of the year remains in good agreement. The annual figures for the primary statistics, presented in Table 4, show that the satellite and ground-based radiometer PWV measurements for Mt. Graham coincide. Erasmus & van Staden (2001) found similarly good agreement at Paranal and Chajnantor.

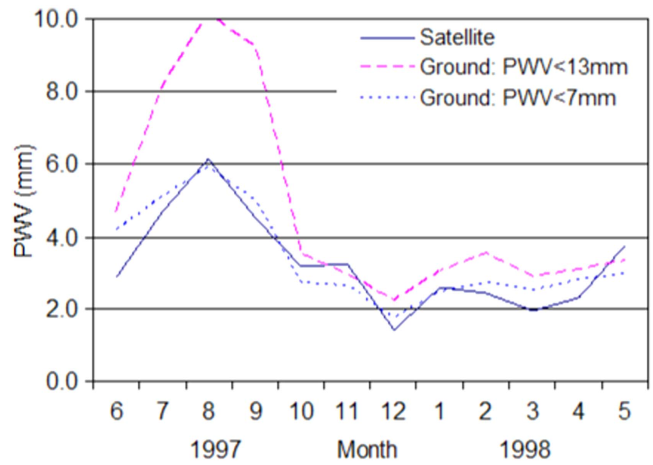

Figure 4. Mean monthly PWV at Mt. Graham for the period 1997 June to 1998 May as determined from satellite and a SMTO ground-based radiometer. Considering only radiometer PWV values less than 7 mm, there is a good agreement between observations.
(A color version of this figure is available in the online journal.)

Table 4
PWV Statistics at Mt. Graham

	PWV (mm)	
	Satellite	Ground PWV < 7 mm
10th Percentile	1.15	1.07
1st Quartile	1.86	1.55
Median	2.60	2.52
3rd Quartile	5.99	3.91

3.4. Cloud Classification and Detection

3.4.1. Cirrus Clouds

Cirrus or high-altitude clouds thickness is inferred from the 6.7 μm imagery. These clouds are found at an altitude of ~9–12 km, higher than the water vapor emission layer that it is at ~4–9 km of altitude. IR radiation from water vapor below the 300 mb level (~9 km) is absorbed and re-emitted at colder temperatures by the cloud particles. Because the relationship between UTH and water vapor brightness temperature defined in Section 3.3 is only valid under clear conditions, the presence of cirrus cloud particles causes UTH values to rise to the point that they are no longer valid. When UTH values rise to around 50%, cirrus cloud particles start forming by condensation and deposition. As UTH values rise further, the cloud particles grow in size and number and the cirrus cloud become thicker. Therefore, when UTH values rise above 50%, the UTH is an indicator of the presence and transparency of cirrus clouds.

Erasmus (2000) and Erasmus & Sarazin (2002) determined the threshold UTH values accurately. They used atmospheric transparency measurements made on the ground at optical wavelengths and compared these with a transparency index based on the satellite UTH measurement. The authors showed that the satellite transparency index does effectively discriminate between photometric and non-photomeric observing conditions as measured by the Line Of Sight Sky Absorption

Monitor (LOSSAM) at La Silla Observatory. The UTH threshold values obtained are the following: clear: UTH $\leqslant$ 50%; opaque: UTH $\geqslant$ 100%, and transparent: 50% $<$ UTH $<$ 100%.

3.4.2. Cloud in the Middle and Upper Troposphere

The 10.7 μm channel data are used to detect cloud in the middle and upper troposphere. Typically, temperature drops with height in the atmosphere. Then, if the pixel temperature T_{ir} is colder than the surface temperature T_s at a given pixel location, it is indicative of the presence of cloud above the surface. However, there are some obstacles for unambiguous cloud detection. First, pixel temperatures T_{ir} need to be referenced against an independent measurement. The surface pressure P_s and corresponding surface temperature T_s, for a given location were estimated by interpolation from the radiosonde data and the terrain height.

The actual surface temperature may be warmer or colder than T_s because there is usually additional cooling at night or warming -during the day- of the air by contact with the ground. First scenario: if the actual temperature is warmer (daytime) than the estimated T_s, cloud detection is not compromised as if cloud is present, even a thin layer near the surface, the cloud top temperature $T_{ir} < T_s$. Let T_r the cloud detection temperature threshold, then if $T_r = T_s$, the presence of cloud is correctly determined. Second scenario: if the actual temperature is colder (nighttime) than the estimated two conditions are possible: (i) cloud may be present or (ii) the ground is cold and is incorrectly being interpreted as cloud. To avoid this problem, a T_r lower than T_s must be used, but the difference between T_r and T_s must be minimized so that cloud, if it is near the ground, does not go undetected.

High-altitude, high-latitude inland sites will exhibit the largest problem with detection of ground in the winter, as this setting maximizes nocturnal ground cooling. In contrast, at sites near the coast, at lower altitudes and at those with well vegetated surfaces the ground cooling effect would be less. In order to optimize the value of T_r, cloudiness observed at different times of the day, for day/night periods, and seasons of the year was analyzed at San Pedro Mártir, Mt. Graham, Sierra Negra, Boundary Peak, and Kitt Peak. These sites represent the range of altitudes, latitudes, and inland extents of existing and potential sites.

For these five sites, T_r was initially based on P_s as computed from the nearest radiosonde sounding and the actual site altitude. Given these conditions, the pressure level on which T_r is based was reduced and increased in a step-wise manner using increments of 10 mbar ($\sim$100 m). At the sites where ground detection is less of a problem, ground detection is absent when the pressure level on which T_r is based was 120 mbar above the surface.

Ground detection was determined by examining the cloud counts for the individual pixels making up a 9-pixel area representing the site. At the level of the tropopause, at about 12 km, for an observer on the ground viewing the sky, this 9-pixel area would correspond to the sky within approximately 60° of zenith as it is illustrated in Figure 5. Evidence for ground detection is readily apparent as an aberrant count in pixel locations corresponding to the highest local terrain. The pressure compensation of 120 mbar is clearly a maximum that corresponds to the greatest ground cooling toward the end of long winter nights. At other times of the night and during other seasons of the year, the required pressure compensation would be less. This was taken into account in the algorithm dealing with the ground detection problem.

Ground detection is eliminated at all sites when the pressure altitude reaches 200 mbar above the surface. The main reason for differences between the sites appears to be the proximity of the radiosonde station to the site. Any differences between sites was represented as an offset pressure between zero and 80 mbar and the remaining 120 mbar was modeled as a layer of variable thickness, a pressure level compensation P_{sc}, in terms of the night length.

3.4.3. Cloud Detection Procedure

If a pixel from the 6.7 μm imagery is determined to have opaque cirrus, then the final cloud cover classification for that pixel location is opaque since the corresponding pixel in the 10.7 μm image would also give an opaque signature. However, if a pixel is either clear or transparent from the 6.7 μm image analysis, the corresponding pixel in the 10.7 μm image is examined. If cloud is detected in that pixel, then the pixel location is classified as opaque; if not, then pixel locations classified respectively as clear or transparent remain clear or transparent.

The clear fraction may be considered as an upper limit for the fraction of time that observing conditions are photometric because (i) sub-pixel scale cloud elements that are sufficiently small and/or sparse may lead to a pixel with such cloud elements being classified clear; (ii) a larger cloud element located partly in two or more pixels may result in the individual pixels being classified as clear if a sufficiently large fraction of the pixels are cloud free; and (iii) pixels with UTH values near the clear-transparent threshold may not be purely photometric.

A more accurate determination of clear—hence, photometric—and partly cloudy—hence, spectroscopic—conditions was made using a cluster of pixels to represent the site instead of an individual pixel. As shown schematically in Figure 5, a 9-pixel area was used to represent the astronomical sky at the site.

The 9-pixel area shown in Figure 5, considered representative of the astronomical "sky" at that site, was used to determine clear and party cloudy conditions. The number of

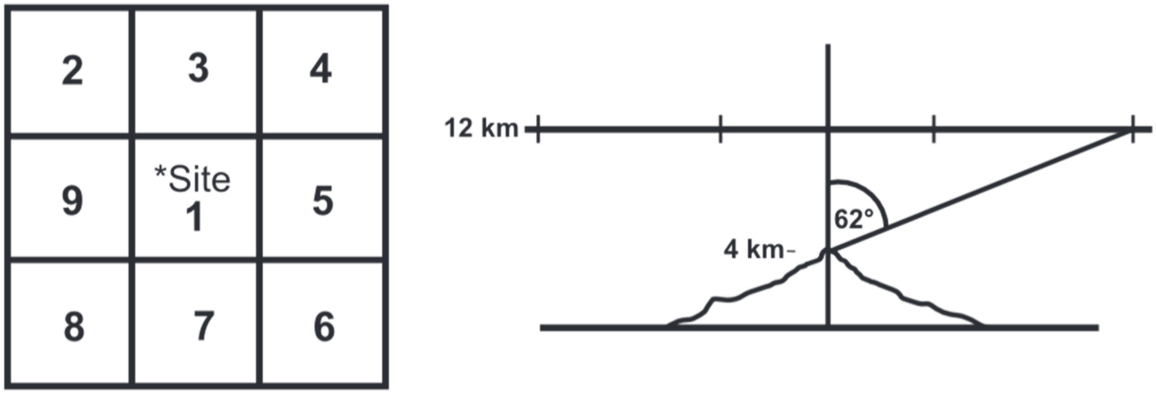

Figure 5. Schematic diagram showing the 9-pixel site area in plan view (left) and cross section (right).

pixels within the area for each cloud cover category was counted, and that count was used to provide a more accurate measure of observing conditions. If cloud elements are in the area, even if most are sub-pixel scale, it is likely that at least one of the 9 pixels will have either a transparent or opaque signature. Thus, if all 9 pixels in the site area are simultaneously clear, one can be fairly confident that observing conditions are indeed photometric. The following classification was used: (i) clear or photometric: 9 pixels are clear; (ii) transitional or spectroscopic: 6–8 pixels are clear; and (iii) opaque or unsuitable for astronomy: 1–5 pixels are clear.

To verify the accuracy of the satellite measurement of observing quality, a comparison was made with records of observing conditions at San Pedro Mártir Observatory for a one year (Tapia 1992). Using periods of half-nights, conditions were classified as photometric: less than 15% cloud cover or no more than 30 minutes of cloud cover in a 5-hour period, or spectroscopic: more than 15% but less than 65% cloud cover. In some months, for the ground-based observations, less than half of the nights were sampled. For the satellite, observations are made every night, typically three times per night. The annual figures for both photometric and spectroscopic fractions are shown in Table 5. This comparison shows a good agreement between satellite and ground-based measurements of observing conditions for this site. Differences in the fractions obtained for each observing method are consistent with differences in the definitions of photometric or spectroscopic conditions. Similar levels of agreement were found at Paranal Observatory (Erasmus & van Staden 2001).

Table 5
San Pedro Mártir Data (1997 June to 1998 May)

Data Type	% Photometric	% Spectroscopic	%Usable
Satellite	69.8	11.8	81.6
Ground	67.5	15.6	83.1

3.5. Merging of the Meteosat-3 and GOES-8 Data Sets

A merging of the Meteosat-3 and GOES-8 data into one contiguous data set that is internally consistent was carried out. This procedure was developed and tested for a similar analysis by Erasmus (2000). The procedure included a UTH calibration for the Meteosat-3 data using the Denver radiosonde. This calibration provides a smooth transition across the time boundary of the two data sets as can be seen in Figure 6. It is shown the monthly PWV values for four sites in the USA as derived from the two satellites in the period 1993 July 1993 to 1996 February where the transition occurred in 1995 January. The PWV values for the sites were derived as described in Section 3.3. Site values are for clear conditions from the site altitude upward. Denver radiosonde PWV is for all conditions from the 600 mbar pressure level (4400 m) upward. The three sites shown in this figure are in geographically and climatologically diverse regions, yet at all the sites the transition between the data sets is seamless.

3.6. Climatological Representativeness of the Study Period

To assess the study period of 6 years in terms of long-term trends and inter-annual climate variability, the data set of the National Centers for Environmental Prediction (NCEP) and National Center for Atmospheric Research (NCAR) reanalysis, Kistler et al. (2001) was used. It is a retroactive reconstruction of atmospheric parameter fields extending back more than 40 years. Historical data from all possible sources were collected and added to existing databases. Data then underwent an extensive quality control. An assimilation scheme, kept constant over the reanalysis period, was then used to interpolate the observations to a global grid at $2\overset{\circ}{.}5 \times 2\overset{\circ}{.}5$ resolution

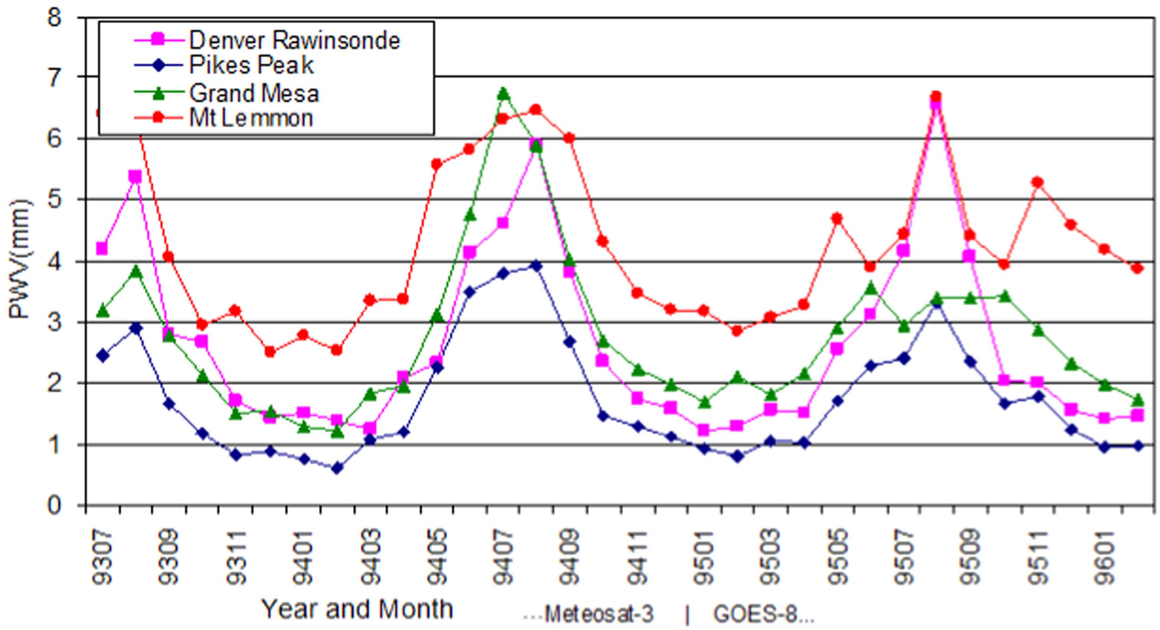

Figure 6. Mean monthly PWV at selected sites as derived from Meteosat-3 and GOES-8 satellites. The transition between the two data sets is 1995 January. (A color version of this figure is available in the online journal.)

(Kistler et al. 2001). A file containing 41 years of selected monthly parameters has been produced from the full resolution data set. The parameters analyzed were the out-going long-wave radiation (OLR) at the top of the atmosphere and the 500 mbar specific humidity q.

3.6.1. Out-going Long-wave Radiation and Cloud Cover

Cloud cover is inversely related to ORL [Wm^{-2}] as an increase in cloud cover will reduce the ORL reaching the top of the atmosphere from the Earth's surface and vice versa. Four sites were chosen to be representative of the main climatic regions of interest: west coast subtropical (San Pedro Mártir), interior subtropical (Mt. Graham), the subtropical-tropical margin (Sierra Negra), and the subtropical-temperate margin (Boundary Peak). The closest grid points in the NCEP-NCAR reanalysis data set used for each of the sites are presented in Table 6.

Mean monthly values of OLR over the 41-year period from 1958 to 1998 were used. First, the 12-month running mean was computed to remove the seasonal cycle and these data were used to determine the 41-year trend. Second, the monthly anomalies were determined by subtracting the 41-year mean for a given month from the individual monthly values. The rms difference between the individual monthly means and the 41-year mean is used as an indicator of the inter-annual variability. The results are shown in Table 7.

Figures 7 to 10 show the trend and anomaly plots for OLR at the four sites. The long-term trend in OLR suggests upward at San Pedro Mártir, Sierra Negra, and Boundary Peak. However, an accurate determination of the OLR is enhanced when satellite observations are used. If the trend line is based on data collected after the advent of satellite observations, i.e., 1978 to 1998, the trend is either reversed in the case of San Pedro Mártir or much reduced for Sierra Negra and Boundary Peak, while Mt. Graham shows no clear trend in OLR. Inter-annual variability is large compared to the long-term trend. At Sierra Negra, the site with the largest long-term trend, there was an increase in OLR over the period 1978 to 1998 of 6.6 Wm^{-2}, while the typical inter-annual variability was 10.8 Wm^{-2}.

At all the sites variability within the study period is comparable to long-term values. At Mt. Graham the mean OLR was also similar to long-term values. However, at the other three sites there was a greater difference between the mean for the study period and the long-term means. Given the reliability of pre-1978 OLR, the assessment of the study period was based on a comparison with 1978-1998 data.

Table 6
Site Coordinates and NCEP Grid Points used in the Climate Analysis

Site	Elevation	Sites		Grid point	
	m	Lat N	Long W	Lat N	Long W
San Pedro Mártir	3069	31.04	115.45	30	115
Mt. Graham	3268	32.70	109.87	32.5	110
Sierra Negra	4581	18.98	97.30	20	97.5
Boundary Peak	4003	37.85	118.35	37.5	117.5

Table 7
ORL (Wm^{-2}) Means, Trends (ΔOLR), and Variability (rms) at Four Sites

Site	58–98 Mean	78–98 Mean	93–99 Mean	58–98 ΔOLR	78–98 ΔOLR	58–98 rms	78–98 rms	93–99 rms
San Pedro Mártir	287.4	289.0	286.6	3.8	−4.6	8.82	8.72	9.87
Mt. Graham	258.2	258.7	258.0	−0.7	−1.5	9.15	8.88	9.47
Sierra Negra	264.7	268.6	269.1	15.8	6.6	12.22	10.81	10.24
Boundary Peak	258.1	261.6	264.0	11.18	4.13	9.44	8.78	9.38

Table 8
500 mbar Specific Humidity (g/kg) Means, Trends, and Variability at Four Sites

Site	58–98 Mean	78–98 Mean	93–99 Mean	58–98 Δq	78–98 Δq	58–98 rms	78–98 rms	93–99 rms
San Pedro Mártir	0.77	0.75	0.76	−0.025	0.014	0.21	0.21	0.21
Mt. Graham	1.49	1.49	1.39	−0.020	−0.300	0.31	0.29	0.29
Sierra Negra	1.71	1.61	1.65	−0.394	−0.252	0.42	0.39	0.39
Boundary Peak	0.87	0.84	0.82	−0.096	−0.072	0.17	0.16	0.16

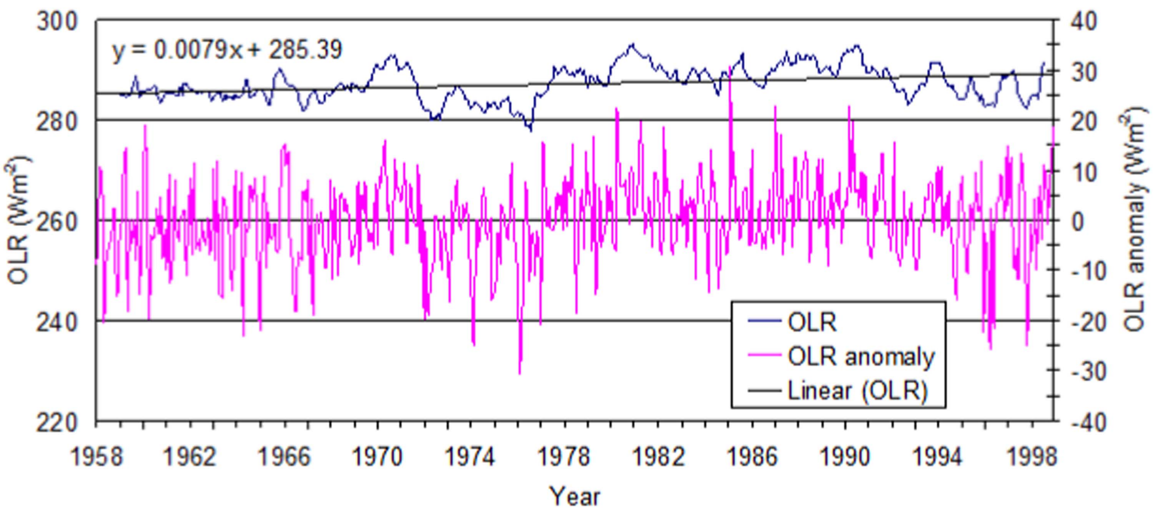

Figure 7. 12-months' mean ORL and ORL anomaly at San Pedro Mártir.
(A color version of this figure is available in the online journal.)

The relationship between monthly OLR values and the monthly cloud cover anomalies during the study period were analyzed for San Pedro Mártir. This site was chosen since the site and NCEP grid point are in reasonably close proximity, as shown in Table 6 and both were found to lie within the same clear fraction isokeph in the area analysis as will be discussed in Section 4. From Figure 11 on a month-to-month basis, there is not exact correspondence between the clear fraction anomaly and OLR anomaly. This is not unexpected since the satellite measurement is based on cloud cover above the observatory at ∼10 km resolution while the OLR is for the grid point location in the NCEP data domain at 2°5 resolution. Additionally, surface altitude is different and the locations are separated by a distance of about 120 km. The usefulness of the comparison lies in assessing average, i.e., climatological conditions, over the entire study period. The rms difference between the monthly means and the individual monthly values for the clear fraction anomaly is 9.9% while the NCEP ORL rms anomaly is 8.8 Wm^{-2}. To a first approximation, an OLR anomaly of 1 Wm^{-2} corresponds to a cloud cover anomaly of about 1%. Therefore, using the period 1978-98 as a baseline, it follows that the clear fraction is being overestimated at San Pedro

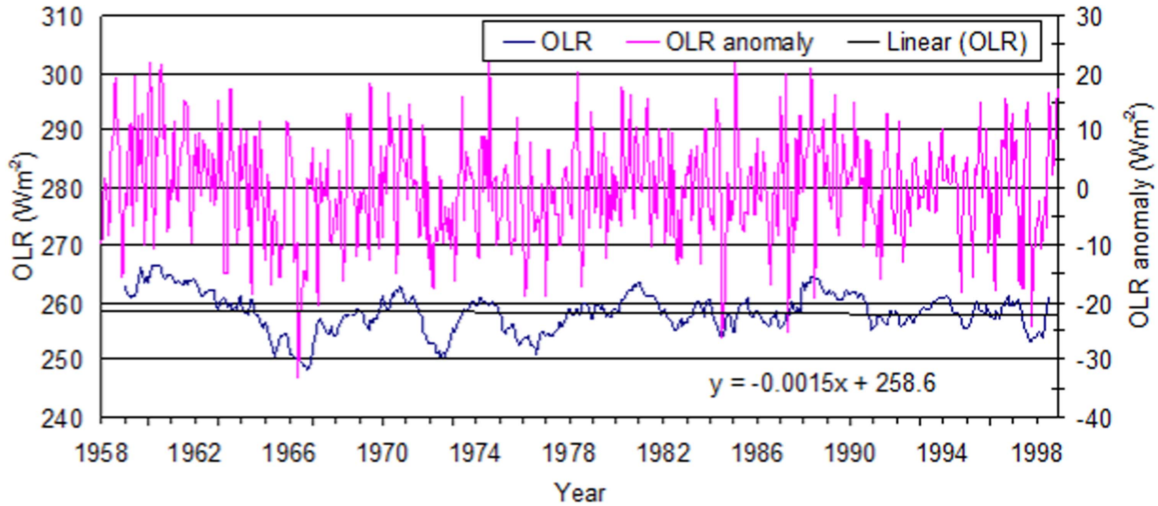

Figure 8. Twelve-month mean ORL and ORL anomaly at Mt. Graham.
(A color version of this figure is available in the online journal.)

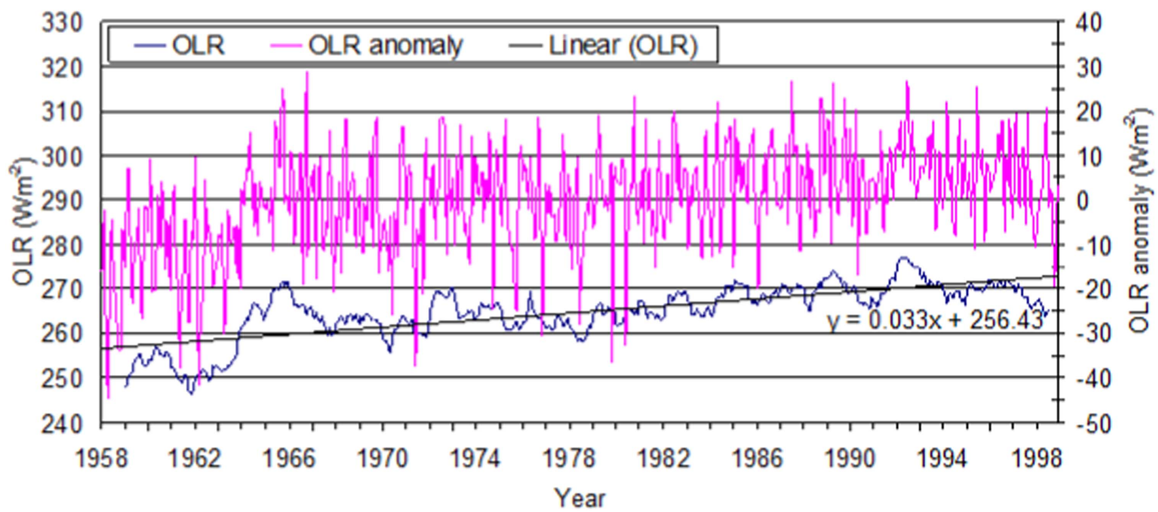

Figure 9. Twelve-month mean ORL and ORL anomaly at Sierra Negra.
(A color version of this figure is available in the online journal.)

Mártir and underestimated at Boundary Peak by ~2% at each site during the study period.

3.6.2. Specific Humidity and PWV

The specific humidity [g/kg] is a quantity closely related to the water vapor mixing ratio, see Section 3.3. Being the mass of water vapor [g] in a kilogram of air, it is an absolute humidity measurement proportional to PWV. At the 500 mbar pressure level, q is indicative of moisture conditions in the middle troposphere. Mean monthly values of 500 mbar q over the 41-year period from 1958 to 1998 were used. Figures 12 to 15 show the 500 mbar specific humidity trend and anomaly plots for the four sites. Sierra Negra and Boundary Peak have downward trends over both the 41-year and 21-year periods. This is consistent with the upward trend in ORL at these sites. Mt. Graham shows a downward trend over the period 1978-98. San Pedro Mártir is the most stable site in the long term, which is consistent with the fact that this is a coastal site under oceanic influence.

At all sites, the inter-annual variability during the period is comparable to the long-term values. Comparing the mean for the study period with the long-term means at Mt. Graham and Boundary Peak the study period was drier than normal. At Sierra Negra, the study period was comparable to conditions in the last 20 years but drier than the 41-year average. Since PWV

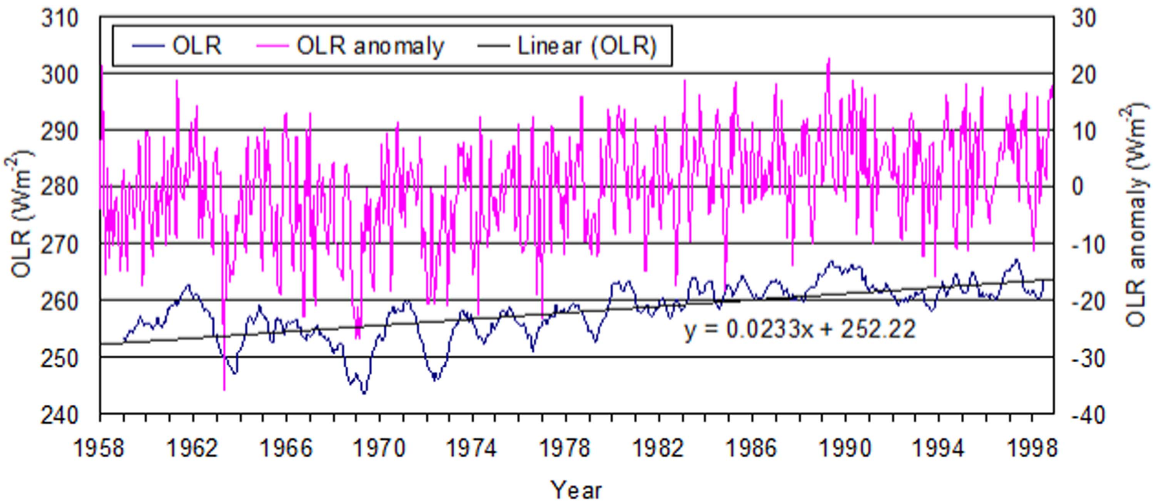

Figure 10. Twelve-month mean ORL and ORL anomaly at Boundary Peak.
(A color version of this figure is available in the online journal.)

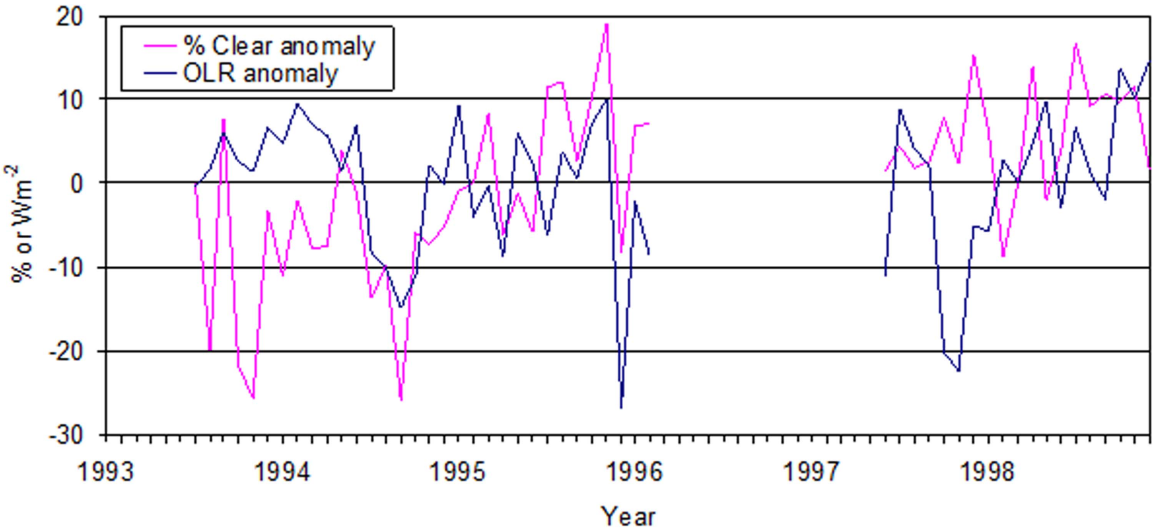

Figure 11. Monthly clear fraction and ORL anomalies at San Pedro Mártir.
(A color version of this figure is available in the online journal.)

is directly proportional to q, then it follows that PWV values were underestimated at Mt. Graham (~7%), Boundary Peak (~6%) and Sierra Negra (~3%) during the study period.

4. Results of the Area Analysis

4.1. Cloud Cover

The general pattern of cloudiness over the area of study was analyzed by producing maps of cloud cover, see Figure 16. The pattern obtained is consistent with the meteorology. Cloud cover is a minimum in the subtropics, 28°N to 35°N, where high pressure prevails for most of the year. Cloudiness increases to the north of these latitudes due to the increasing frequency of winter storms and mid-latitude cyclones, and to the south due to greater tropical storm activity in the summer like cyclones, depressions, monsoonal disturbances, and local convection. Over the land, there is also a general increase in cloudiness from west to east. This is consistent with the fact that, in the subtropics, high pressure is a more permanent feature off the west coast of the continents. This is the case because cold ocean temperatures inhibit rising motion in the atmospheric boundary layer (surface to 1000 m), allowing subsidence to prevail above this layer. On the other hand, areas east of the continental divide are influenced by strong surface

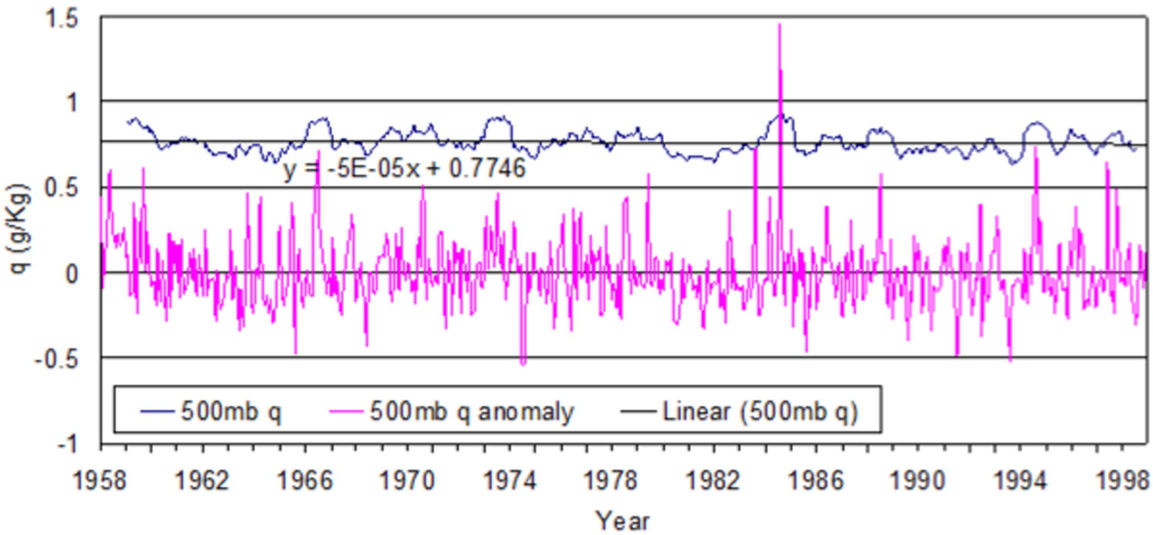

Figure 12. Specific humidity q, 12-month mean and anomaly at San Pedro Mártir.
(A color version of this figure is available in the online journal.)

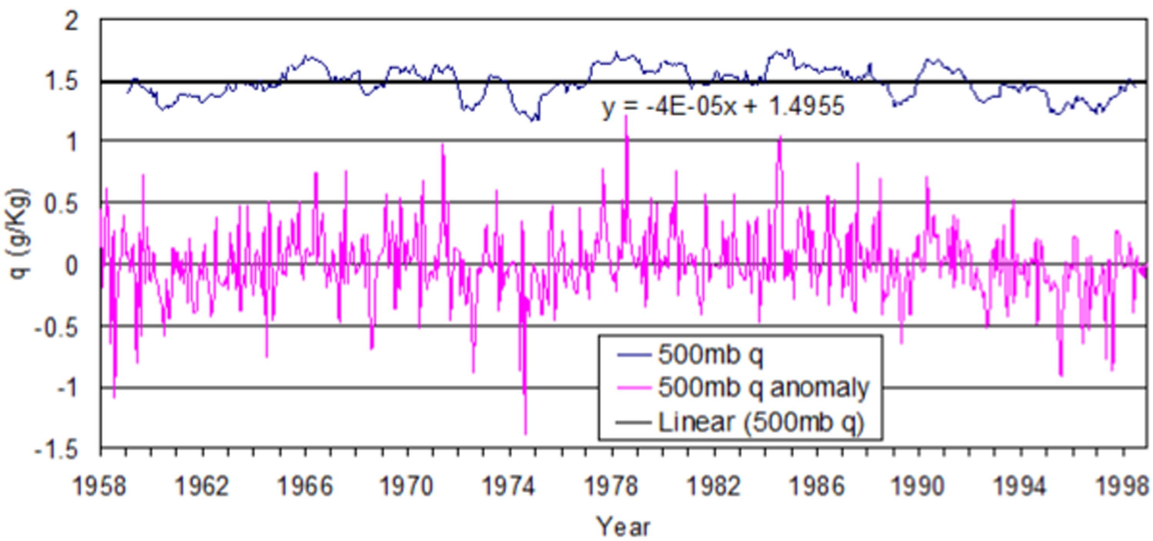

Figure 13. Specific humidity q, 12-month mean, and anomaly at Mt. Graham.
(A color version of this figure is available in the online journal.)

heating over the land and moisture off the Gulf of Mexico. These conditions favor rising motion and cloud formation.

For the observing night, a large area with a clear fraction of 70% or more is observed over southern California, western Arizona, and northern Baja, Mexico. In Baja this area is about 50 km wide extending along the spine of the peninsula northward of 28°N. Small pockets where the clear fraction reaches 75% are found in this region at 30°N, 31°N, and 32.5° N. The area where the clear fraction exceeds 70% extends into the desert interior of southern California. North of this large area, small pockets are observed in the southern Sierra Nevada with clear fractions of 70% or 65%. Westward of the best area described above, a steep gradient of cloudiness is observed near the coast. Coastal cloud associated with fog and low cloud formation below the inversion layer extends inland. At night, the inland extent is determined by local circulation patterns and whether the terrain extends above the height of the inversion layer. This cloud is generally confined to within 50 km of the coast at night.

Inland, a significant cloudiness increase is observed toward the east and north. At about 33°N, traversing Arizona from west, 115°W, to east, 109°W, there is a 20% decrease in the

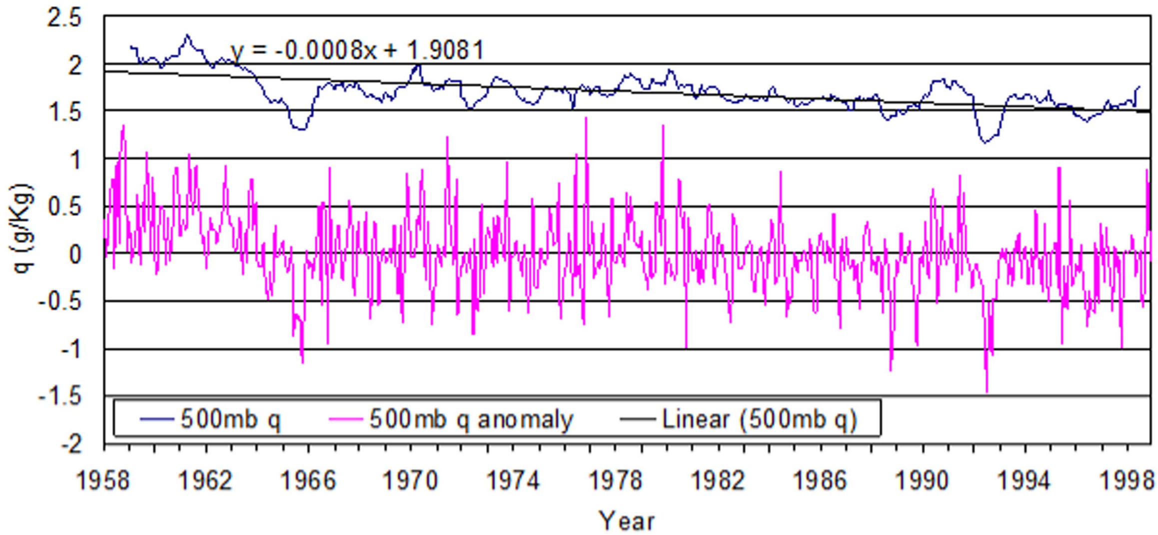

Figure 14. Specific humidity q, 12-month mean, and anomaly at Sierra Negra.
(A color version of this figure is available in the online journal.)

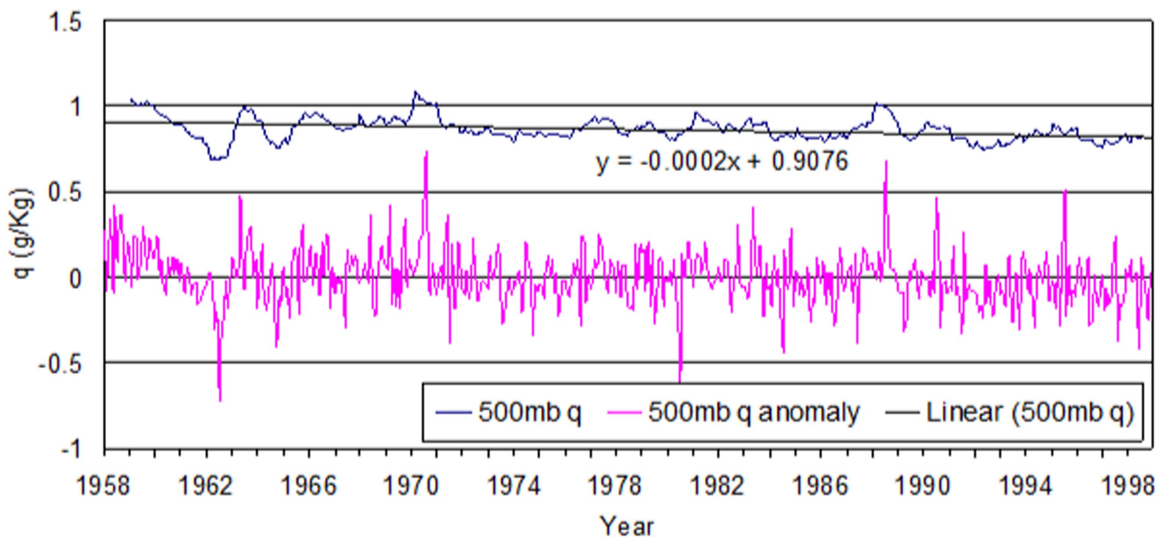

Figure 15. Specific humidity q, 12-month mean, and anomaly at Boundary Peak.
(A color version of this figure is available in the online journal.)

clear fraction. In general, north of the optimal area, cloud cover increases due to the increasing frequency of occurrence of winter storms. However, two pockets where the clear fraction exceeds 65% and 70%, respectively, are found in the southern Sierra Nevada.

Considering the sites in the preliminary list, San Pedro Mártir Observatory and San Gorgonio Mountain lie within the large 70% clear area. Mt. Pinos and Telescope Peak are located on or near the 70% clear isokeph. The 70% clear pocket in the southern Sierra Nevada is in close proximity to Olancha Peak. Near the 65% clear isokeph Hualapai Peak and Kitt Peak. Mt. Palomar lies at the edge of the coastal cloud zone. It appears to be near the 70% clear isokeph but this can not be determined with certainty from the area maps. An additional site, not in the preliminary list, has been identified within the 70% clear isokeph, namely, San Jacinto Peak. The optimal clear area reaches its maximum northward extent at 117°W. A pocket where the clear fraction exceeds 65% is found in this location. A site in or near this pocket, Grapevine Peak (2661 m, 36.9°N, 117.14°W), has been added to the list of sites to be compared. The 10 sites mentioned above were included in the list of sites to undergo a detailed site analysis.

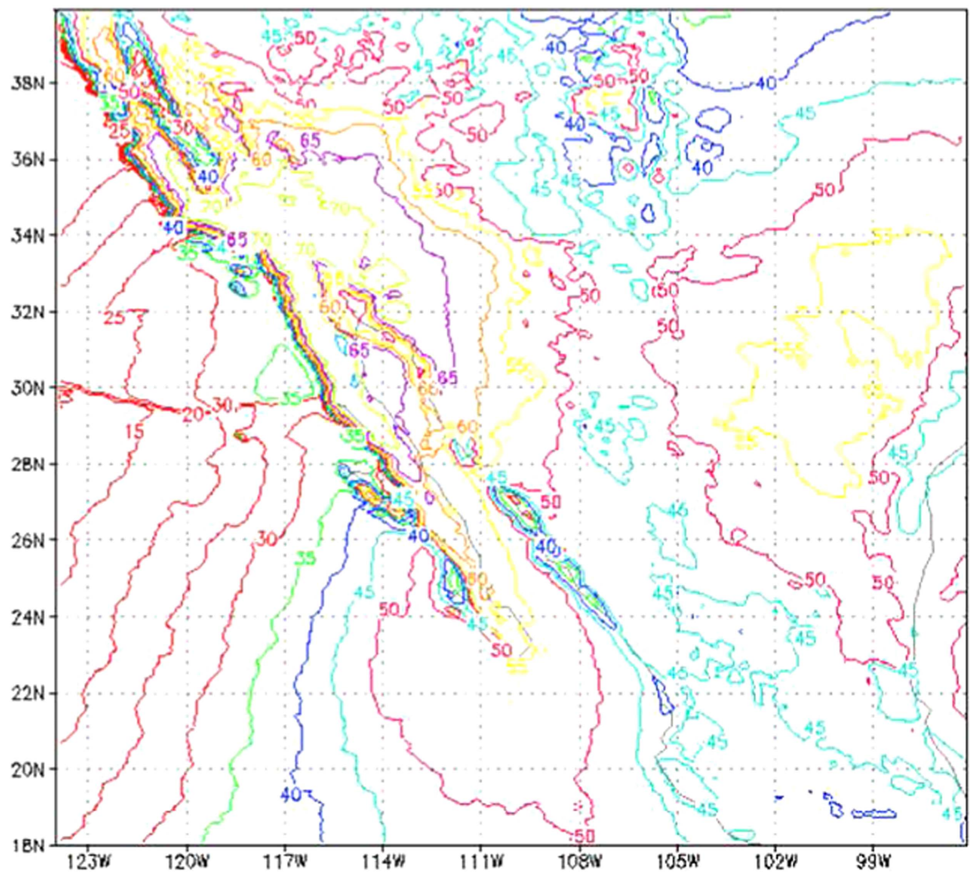

Figure 16. Percentage of clear fraction for the observing night over the study period.
(A color version of this figure is available in the online journal.)

Examination of the map of the usable fraction (not shown) i.e., clear plus transitional cloudiness, indicates the same general pattern as the clear fraction map. Over the areas that are generally clear i.e., clear fraction >65%, the transitional cloud fraction varies only slightly, being about 10%. An interesting exception was found just north of the optimal area in the Sierra Nevada range where the transitional fraction is higher, over 15%. This is almost certainly due to ground being detected over the very high peaks in this area. Thus the clear fraction for sites in this area may be up to 5% higher than indicated in the clear fraction map. This consideration and the low PWV values led to the inclusion of Boundary Peak located in the Inyo Mountains.

The map of the daytime clear fraction (no shown) reveals the same general pattern of cloudiness. In general, daytime clear fractions are slightly higher than nighttime clear fractions. Large differences between daytime and nighttime cloudiness are observed in inland valleys where daytime heating leads to cloud dissipation.

Analysis of maps for the four day-night periods show that diurnal variations in cloudiness are smaller in the west and larger in the east. This is consistent with the fact that cloudiness in the west is largely stratiform in nature whereas in the east the convective cycle dominates. Stratiform clouds are produced by large-scale weather systems which are less affected by the diurnal heating and cooling cycle. Some dissipation of low-level stratiform cloud occurs in the daytime, resulting in a larger clear fraction. This is particularly noticeable along the west coast and in adjacent inland valleys. Convection dominates along the main mountain ranges and to the east. Clouds tend to form in the mid to late afternoon, especially in arid regions. Thunderstorms develop and continue to exist into the evening hours. Following dissipation of these storms, thick high-altitude cloud (anvil cirrus) may linger till after mid-night. By early morning, these clouds have dissipated.

4.2. Precipitable Water Vapor

PWV above a site is controlled to a very large degree by altitude. Higher sites are dryer because the scale height for water vapor in the atmosphere is small and higher sites are colder. To evaluate PWV within the context of the cloud cover analysis the percentage frequency of occurrence of PWV

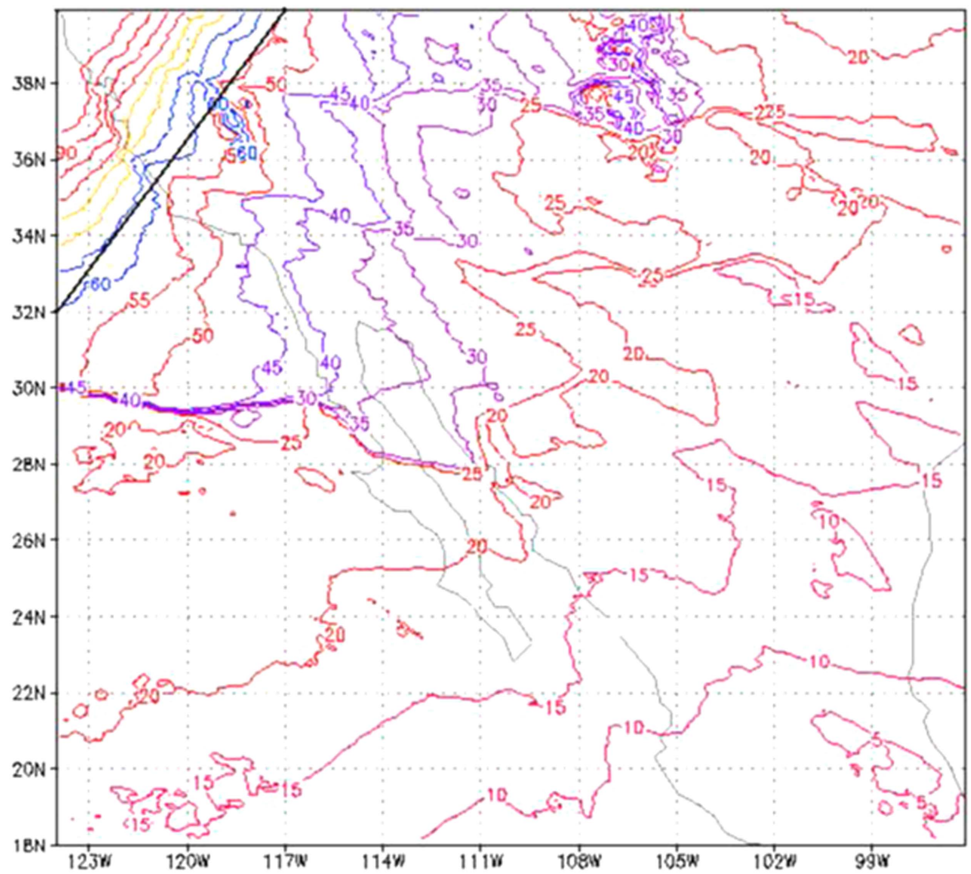

Figure 17. Frequency of occurrence (%) of PWV values less than 2 mm in the atmospheric layer above 700 mbar pressure level, equivalent to ~3300 m, for the observing night, over the study period.

(A color version of this figure is available in the online journal.)

observations below selected thresholds were created for clear conditions. PWV is computed for the layer of the atmosphere above the 700 mbar pressure level, equivalent to ~3300 m or the surface if the surface pressure is lower than 700 mbar. The presumption is that a site being sought for low PWV levels will necessarily be a high-altitude site. Because this parameter is so critically dependent on site altitude and since smoothed digital terrain heights are used in the area analysis, the PWV maps were only used for general assessment.

Regional pattern maps of water vapor were produced showing the percentage frequency of occurrence of PWV values below 3 mm, 2 mm and 1 mm. Figure 17 shows the map obtained for values less than 2 mm for the observing night. A decrease in PWV from the southeast to the northwest was observed that is primarily due to the equator-pole temperature gradient and second to the east-west moisture gradient. In the corresponding maps below, 1 mm (not shown) and 2 mm a localized PWV minima was observed over the highest terrain in the Rockies, Sierra Nevada, and southern Sierra Madre Oriental. Because of the digitized terrain heights used in the area analysis, the exact location of the PWV minima and the exact percentage frequency of low PWV values at these minima can not be deduced from this analysis. The same applies at isolated high-altitude peaks; accordingly, two high-altitude site were included in the list of sites, Sierra Negra at 4581 m and Pikes Peak at 4298 m.

4.3. Site Selection

As a result of the analysis described in the previous section, the 11 best sites in terms of the clear and usable fractions for the observing night were identified. The remaining four sites that were included in the comparison were selected on the basis of other criteria. Mt. Graham was included since it is an existing observatory. Co. Santiago in the southern tip of the Baja peninsula was included as the most promising site for optical astronomy in Mexico after San Pedro Mártir. The final two sites, Sierra Negra, and Pikes Peak, were selected on the basis of their low PWV conditions and hence their suitability for infrared and millimeter astronomy. These 15 sites selected for further analysis and comparison are listed in Table 9.

Table 9
Existing and Potential Telescope Sites Compared in the Site Analysis

No.	Site	Short name	Altitude (m)	Latitude	Longitude	Remarks
1	Boundary Peak	Boundary	4003	37.846	−118.350	
2	San Gorgonio	Mnt. Gorgonio	3503	34.100	−116.830	
3	Mt. Graham	Graham	3268	32.700	−109.870	Existing observatory
4	Grapevine Peak	Grapevine	2661	36.965	−117.148	
5	Hualapai Peak	Hualapai	2564	35.075	−113.900	
6	San Jacinto	Mtn. Jacinto	3290	33.813	−116.677	
7	Kitt Peak	Kitt	2097	31.963	−111.698	Existing observatory
8	Sierra Negra	La Negra	4581	18.980	−97.300	Existing observatory
9	Olancha Peak	Olancha	3695	36.265	−118.116	
10	Mt. Palomar	Palomar	1871	33.313	−116.860	Existing observatory
11	Pikes Peak	Pikes	4298	38.841	−105.044	
12	Mt. Pinos	Pinos	2692	34.812	−119.146	
13	San Pedro Martir	San Pedro	2800	31.040	−115.450	Existing observatory
14	Co. Santiago	Santiago	2160	23.550	−109.967	
15	Telescope Peak	Telescope	3369	36.170	−117.090	

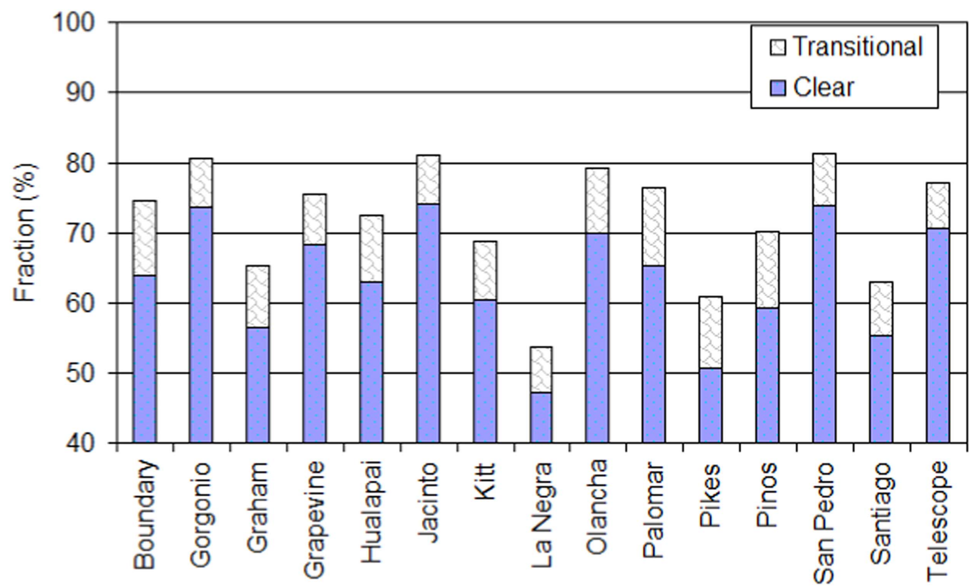

Figure 18. Fraction of clear (photometric) and transitional (spectroscopic) time.
(A color version of this figure is available in the online journal.)

5. Results of the Individual Site Analysis

The sites selected for comparison were analyzed in terms of cloud cover and PWV. The results obtained for overall conditions, seasonal, and diurnal variabilities are presented.

5.1. Cloud Cover

5.1.1. Overall Conditions

The fraction of the time that conditions are clear, transitional, and usable during the observing night are shown in Figure 18. San Pedro Mártir, San Gorgonio Mountain, and San Jacinto Mountain are the clearest sites, all with clear fractions of about 74%. The usable fractions at these three sites are also very similar of ∼81%. The next clearest sites are in the desert interior in and around Death Valley National Park. These are Telescope Peak, Olancha Peak, and Grapevine Peak with clear fractions between 68% and 70%.

The increase in cloudiness moving from west to east is evident in the clear fractions observed at Hualapai Peak (63%), Kitt Peak (60%), and Mt. Graham (56%), respectively. Regarding the lower coastal sites Palomar Mountain at 1871 m, Mt. Pinos, 2692 m and Co. Santiago at 2160 m, the first two have larger clear fractions. This may be explained by

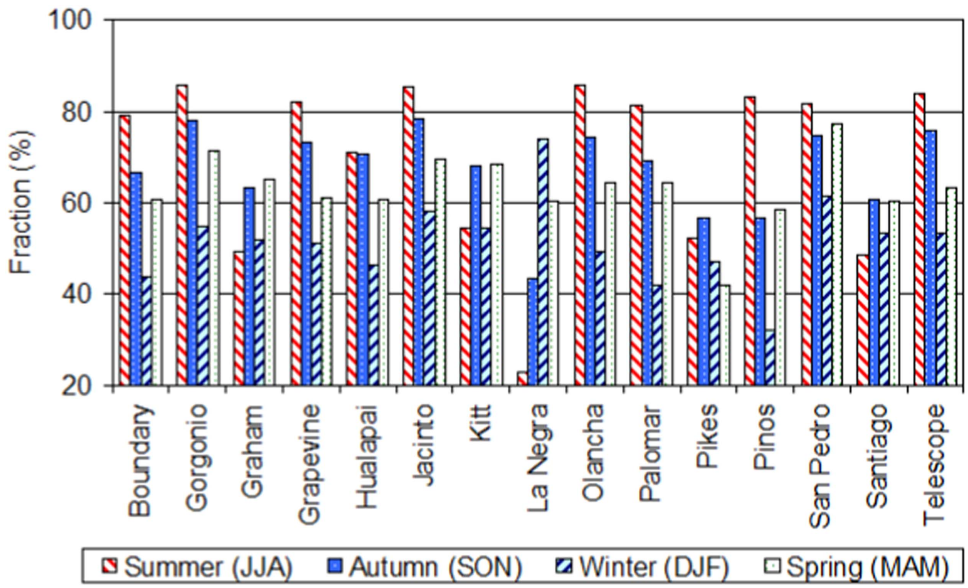

Figure 19. Fraction of night clear (photometric) time by season.
(A color version of this figure is available in the online journal.)

the colder ocean water at the more northerly sites which contributes to a lower inversion height at these locations. However, these low coastal sites are more cloudy than higher sites nearby as San Gorgonio and San Jacinto.

Of the three high-altitude sites -Boundary Peak at 4003 m, Pikes Peak at 4298 m and Sierra La Negra at 4581 m- the first one has by far the largest clear fraction 64%. Note that Boundary Peak and Pikes Peak have relatively large transitional fractions 10.5%. However, an examination of the individual pixel fractions shows that at Pikes Peak the transitional fraction is mostly due to widespread thin cirrus cloud whereas at Boundary Peak the transitional fraction is associated largely with partly cloudy conditions.

5.1.2. Seasonal Variations

The seasonal distribution of clear or photometric conditions for the observing night at each site is presented in Figure 19. There is a shift from the clearest season being summer in the north, e.g., Olancha, to being winter in the south, e.g. Sierra Negra. Interestingly, the clearest sites are those with the smallest seasonal range.

5.1.3. Diurnal Variations

The diurnal cycle of cloud cover, shown in Figure 20, was analyzed by selecting six sites representative of conditions across the study area. Two coastal sites, San Pedro and Santiago, were selected to examine daily variations in coastal cloud cover associated with changes in the inversion height. Four inland sites were selected in a line running, more or less, from northwest to southeast, parallel to the west coast, namely, Boundary Peak, Hualapai Peak, Mt. Graham, and Sierra Negra.

In summer at the two coastal sites, there is an afternoon maximum in cloudiness associated with lifting of the inversion and attendant cloud layer. The effect is particularly noticeable at San Pedro Mártir, where the site is high enough to be located above the inversion at night and in the morning. At Co. Santiago, on the other hand, due to warmer coastal waters, the inversion is much higher, so the site tends to be cloudy for most of the day in summer. At the inland sites, there is also an afternoon cloudiness maximum but this is due to the cycle of convective cloud development. Where convective storms are stronger i.e., adequate moisture at lower levels, cloud tends to linger into the nighttime hours. This is evident at Mt. Graham, Sierra Negra, and Boundary Peak, where the summertime, large-scale circulation pattern favors disturbed weather, cloudiness remains high throughout the day. This is particularly noticeable at Sierra Negra which is influenced by tropical storms moving off the Gulf of Mexico. Mt. Graham also tends to remain cloudy well into the night due to long-lasting convection encouraged by the southwesterly monsoon.

In the autumn months convection is weaker, so more southerly sites like Santiago and Sierra Negra become clearer. In the north, sites begin to come under the influence of mid-latitude cyclones at this time of the year and this tends to increase cloud cover, e.g., Boundary. In the winter, this pattern of cloud enhancement in the north and reduction in the south continues. The result is that Sierra Negra is actually the clearest site in the winter months. With the transition into winter, convective is suppressed with the result that cloudiness

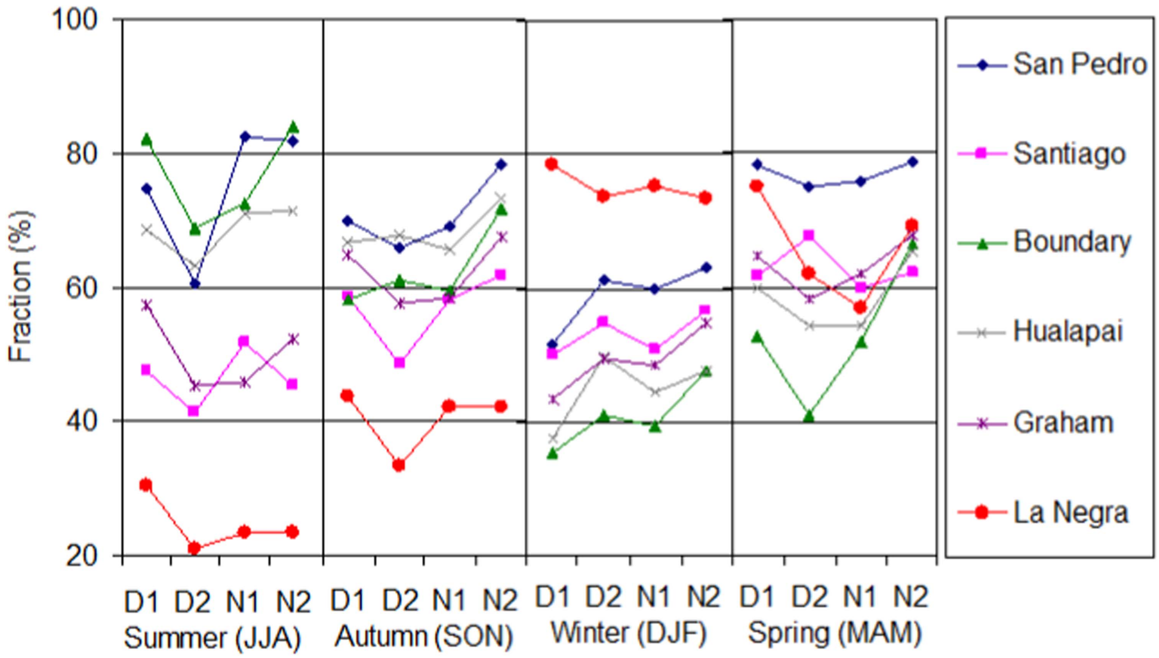

Figure 20. Fraction of clear time for different periods of the day by season. (A color version of this figure is available in the online journal.)

variations through the day remain relatively small. The effect of the convective cycle on cloud cover is observed again in the spring.

5.1.4. Ranking of Sites

For the observing night, a ranking of the 15 sites was carried out based on the (i) clear fraction and (ii) clear plus transitional or usable fraction, respectively. The ranking is obtained by dividing the range of values, clear or usable fraction, into 14 equal intervals. 15 bins were defined with the clear fraction of the clearest site at the center point of bin 1 and the clear fraction of the cloudiest site at the center point of bin 15. Sites are then ranked from 1, clearest, to 15, cloudiest, depending on the bin in which the clear or usable fractions falls, as shown in Table 10.

Table 10
Clear and Usable Fraction Ranking for the Observing Night

No.	Site	Clear Fraction	Rank	Usable Fraction	Rank
1	Boundary	0.640	6	0.746	4
2	Gorgonio	0.737	1	0.806	1
3	Graham	0.563	10	0.654	9
4	Grapevine	0.685	4	0.756	4
5	Hualapai	0.631	7	0.725	5
6	Jacinto	0.742	1	0.811	1
7	Kitt	0.606	8	0.688	7
8	Sierra Negra	0.471	15	0.536	15
9	Olancha	0.701	3	0.793	2
10	Palomar	0.655	6	0.764	3
11	Pikes	0.505	13	0.610	11
12	Pinos	0.594	9	0.703	7
1	San Pedro	0.740	1	0.813	1
14	Santiago	0.553	11	0.631	10
15	Telescope	0.707	3	0.772	3

5.2. Precipitable Water Vapor

PWV is computed when it has been determined that no clouds are present in the 9-pixel site area. This makes sense from an astronomical point of view, because in general clear skies are needed to make observations. PWV was analyzed in terms of overall conditions and seasonal variability.

5.2.1. Overall Conditions

PWV percentile values for the sites are shown in Figure 21 and the PWV frequency distributions in Figure 22. Water vapor in the atmospheric column above a site is strongly related to altitude. This is the case because the scale height of water vapor in the atmosphere is small and because temperature, which determines the water vapor carrying capacity of the air, drops sharply with altitude. The temperature gradient is 6.5°C/km according to the standard model of the atmosphere that considers heat transport. For sites at a similar altitude, differences in PWV are controlled

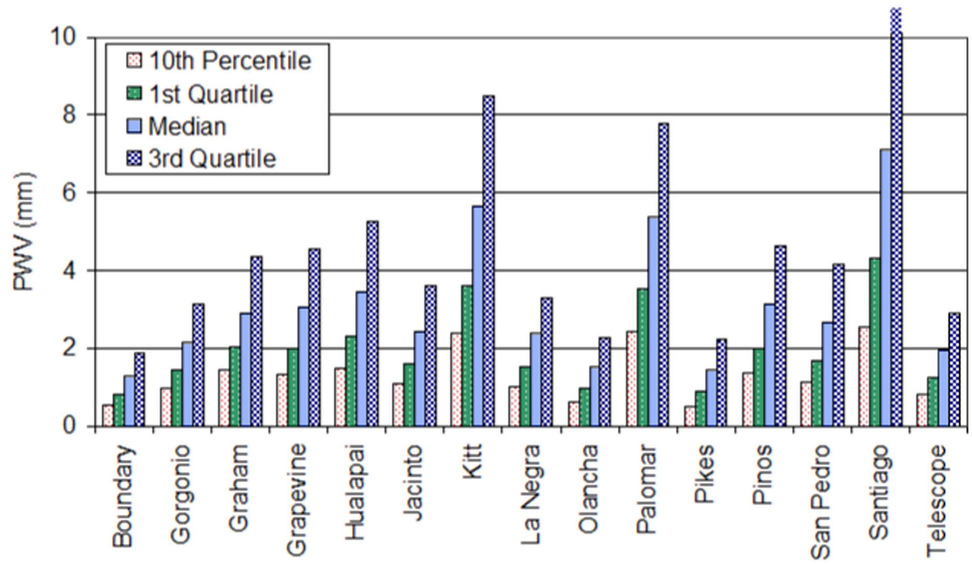

Figure 21. PWV quartiles for all the selected sites.
(A color version of this figure is available in the online journal.)

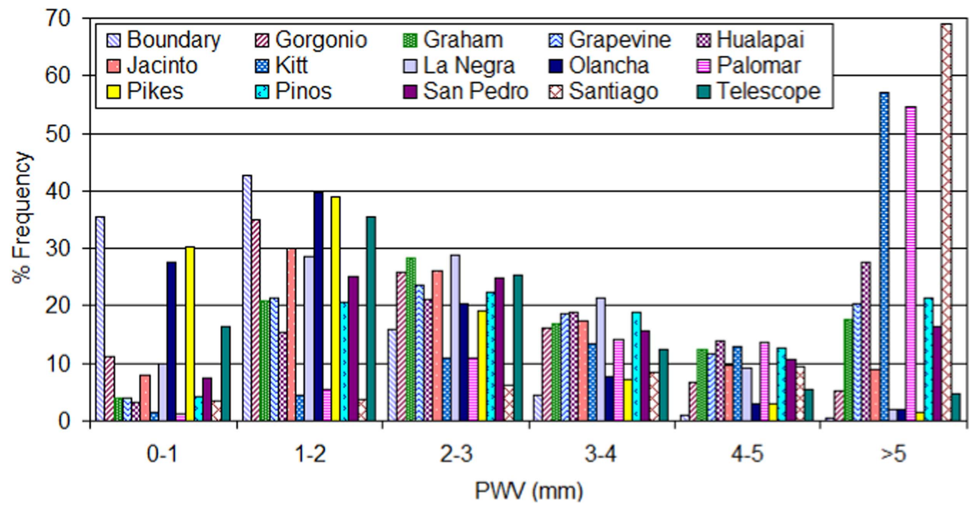

Figure 22. PWV frequency distribution values at each site under clear conditions for the observing night.
(A color version of this figure is available in the online journal.)

by latitude i.e., equator to pole temperature gradient, and moisture advection patterns. Consequently, over the southwestern USA and northern Mexico the large-scale gradient of water vapor is from southeast to northwest. Therefore, Boundary Peak and Pikes Peak have the lowest PWV values. Although Boundary Peak is about 300 m lower than Pikes Peak, it is marginally better since it is located in a drier area west of the Rockies. In view of the general southeast to northwest moisture gradient, Telescope Peak and Olancha Peak are drier than their counterparts with a similar altitude as Mt. Graham and Gorgonio.

5.2.2. Seasonal Variations

The median PWV by season presented in Figure 23 shows that the seasonal variations are generally small. Winter is the driest season and summer is the most humid, as the seasonal temperature cycle is the main control.

For Pikes Peak, mean monthly PWV values were presented in Figure 6. This plot, including Grand Mesa and Mt. Lemmon, illustrates that the merging of the Meteosat-3 and GOES-8 data sets was smooth in geographically and climatologically diverse regions, as described in Section 3.5. Grand Mesa and Mt. Lemmon sites show large PWV seasonal variations; however,

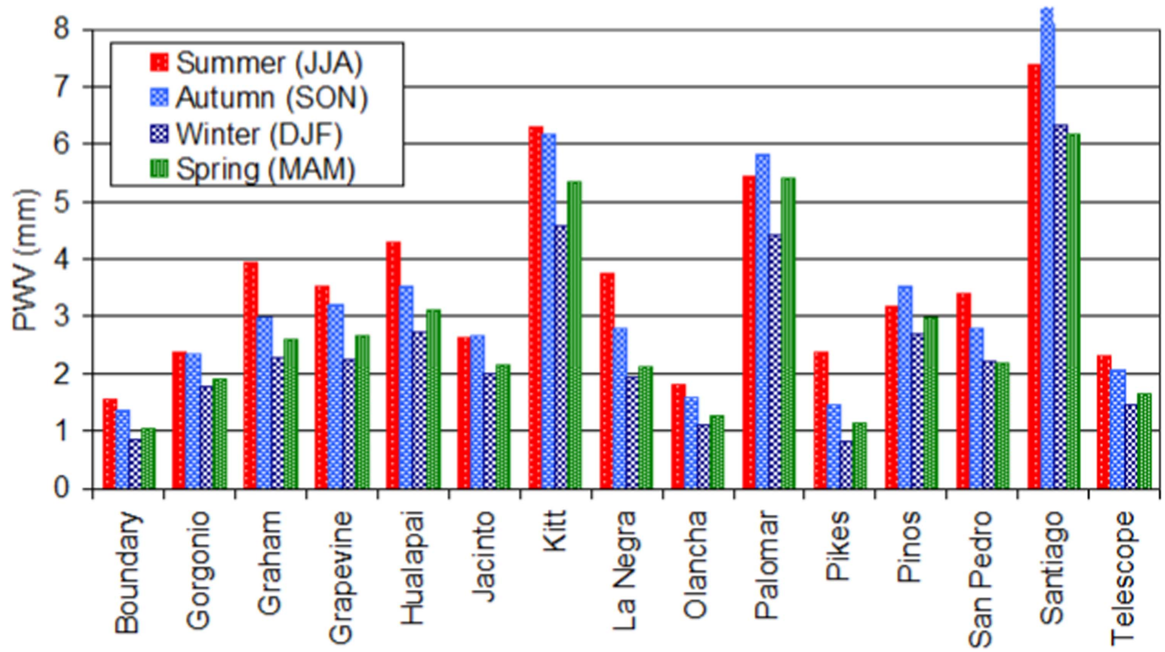

Figure 23. PWV median seasonal distribution at each site under clear conditions for the observing night.
(A color version of this figure is available in the online journal.)

these sites were not included in the area nor in the individual site analysis. The results for Pikes Peak are consistent with those presented in Figure 23. Note that in Figure 6 mean monthly PWV for 31 months are reported while in Figure 23 median PWV by season, obtained from data spanning 58 months, are shown.

5.2.3. Ranking of Sites

PWV measurements were carried out when it was clear. Consequently, if two sites have similar distributions the clearer site is superior. The figures of merit weight the PWV values using the clear fraction at each site. The PWV values and corresponding clear fractions were divided by season of the year in the computations. Two figures of merit based on the median and 10th percentile values of PWV for the observing night were derived for each site as follows:

$$Q1 = (1/PWV_{median})(Clear\ fraction)(100), \quad (3)$$

$$Q2 = (1/PWV_{10thpercentile})(Clear\ fraction) \times (Q1_{mean}/Q2_{mean})(100). \quad (4)$$

Q2 is normalized using the means for Q1 and Q2 at all the sites. Thus, Q1 and Q2 are considered to have equal weight. The ranking is obtained by dividing the range of values into 14 equal intervals. Fifteen bins were defined with the largest Q-value at the center point of bin 1 and the lowest Q-value at the center point of bin 15. Sites are then ranked from 1 to 15 depending on the bin in which the Q-value for the site falls.

Table 11
PWV Percentile Values (mm), Weighted by Clear Fraction

No.	Site	Median	Q1	10%	Q2	QS	Rank
1	Boundary	1.27	212	0.54	210	211	1
2	Gorgonio	2.14	138	0.97	135	136	7
3	Graham	2.88	81	1.43	72	77	12
4	Grapevine	3.04	92	1.33	87	89	11
5	Hualapai	3.46	73	1.49	73	73	12
6	Jacinto	2.40	124	1.09	118	121	8
7	Kitt	5.64	44	2.39	43	44	14
8	Sierra Negra	2.40	88	1.00	85	87	11
9	Olancha	1.52	191	0.61	202	196	2
10	Palomar	5.36	48	2.43	45	47	14
11	Pikes	1.45	154	0.51	159	157	5
12	Pinos	3.13	74	1.35	73	73	12
13	San Pedro	2.67	114	1.14	116	115	9
14	Santiago	7.12	32	2.56	42	37	15
15	Telescope	1.94	148	0.80	152	150	6

The ranking of the sites, values for the median, and 10th percentile, Q1, Q2, and QS = (Q1+Q2)/2 are shown in Table 11.

6. Summary and Conclusions

As part of the preparatory work for the TMT site testing in situ measurements, a series of satellite studies were carried out to reliably compare potential sites. The site for the TMT was decided in 2009. Nevertheless, the TMT site testing team kindly accepted to make public the results, as they can also be useful for the community. In this paper, we described the results of satellite observations spanning from 1993 July to 1999 September used to survey the cloud cover and PWV conditions in the Southwestern USA and northern Mexico.

For an initial analysis in an area that covers 18°N to 40°N and 96°W to 124°W, 33 sites were selected based in precipitation, topography, and climatology, exclusively: seven in California, seven in Arizona, seven in Nevada, and 12 in Mexico. For this area of study, cloud cover and PWV were derived from data of 10.7 μm and of 6.7 μm satellite channels and of rawinsondes, released routinary near the sites of interests. The clear fraction (%) and PWV results were presented in maps. The climatological representativeness of the study period was discussed by analyzing the ORL mean monthly values over a 41-year period in five sites with the main climatic regions of interest, using the NCEP-NCAR reanalysis data set.

As a result of the area of study analysis, 15 sites, including some existing observatories, were further analyzed, compared and ranked in terms of their observing quality. The clearest sites are mountain peaks above the trade wind inversion located along the spine of the Baja peninsula and into southern California between about 28°N and 34°N. A steep gradient of cloudiness is observed along the coast where cloud and fog are trapped below the inversion layer. Inland, a significant cloudiness increase is observed from west to east. At about 33°N, traversing Arizona from west to east, from ~115°W to ~109°W, there is a 20% decrease in the clear fraction. Of the 15 sites compared, San Pedro Mártir, San Gorgonio Mountain, and San Jacinto Peak have the largest clear fraction of ~74%. Telescope Peak and Olancha Peak have clear fractions of 70% or more. The site with the optimal combination of clear skies and low PWV is Boundary Peak. The next best site is Olancha Peak. Pikes Peak has PWV values comparable to Boundary Peak, but is considerably more cloudy.

The results presented in this paper were based in a study funded by the CELT project (University of California and California Institute of Technology). The data were purchased by Cerro Tololo Inter-American Observatory, the University of Tokyo, and the European Southern Observatory. Mt. Graham International Observatory (University of Arizona); the Observatorio Astrónomico Nacional de San Pedro Mártir and the Instituto de Astronomía (Universidad Nacional Autónoma de México); and the South African Astronomical Observatory are also acknowledged for their support.

References

Erasmus, D. A. 2000, Final Report, Rocky Mountain Observatories Consortium. A Satellite Survey of Water Vapour and Cloud Cover at Selected Existing and Potential Infrared Telescope Sites in the Southwestern USA
Erasmus, D. A., & Sarazin, M. 2002, Astron. Soc. Pac. Conf. Ser., 266, 310–26
Erasmus, D. A., & van Staden, C. A. 2001, A Satellite Survey of Water Vapor and Cloud Cover in Northern Chile. Final Report. Cerro-Tololo Inter-American Observatory
Kistler, R., Kalnay, E., Collins, W., et al. 2001, M. Bull. Amer. Meteor. Soc., 82, 257–67
Nelson, J. 2000, in Proceedings of the SPIE, 4004, p. 282–9
Nelson, J. E., & Mast, T. S. 1999, in ESO Conf. WS. Proc. 57, Backaskog Workshop on Extremely Large Telescopes, ed. T. Andersen, A. Ardeberg, & R. Gilmozzi (Garching: ESO), 1
Schöck, M., Els, S., Riddle, R., et al. 2009, Thirty Meter Telescope Site Testing, PASP, 121, 384–95
Sarazin, M. 1991, Air temperature cycles at Paranal. VLT-TRE-ESO-17440-0001, Rev., 1
Soden, B. J., & Bretherton, F. P. 1993, J. Geophys. Res., 96, 16669–88
Soden, B. J., & Bretherton, F. P. 1996, J. Geophys. Res., 101, 9333–43
Tapia, M. 1992, RMxAA, 24, 179–86
Weinreb, M. P., Jamison, M., Fulton, N., et al. 1997, Appl. Opt., 36, 6895–904